# Milestone 4 Final Report: Narrowband Contrast Testbed Demonstration of Hybrid Lyot Coronagraph for WFIRST-AFTA

**Byoung-Joon Seo[a], Brian Gordon[a], Brian Kern[a], Andy Kuhnert[a], Dwight Moody[a], Richard Muller[a], Ilya Poberezhskiy[a], John Trauger[a], and Daniel Wilson[a]**
[a] Jet Propulsion Laboratory, California Institute of Technology, Pasadena, CA. 91109

**Contents**



## 1 Overview

WFIRST Coronagraph technology Milestone 4 was defined as:

> *The Hybrid Lyot Coronagraph (HLC) in the High Constrast Imaging Testbed (HCIT) demonstrates* $1 \times 10^{-8}$ *raw contrast with narrowband light at* $550\,\text{nm}$ *in a static environment.*

In this report, we will present results that meet this milestone definition and demonstrate repeated convergence below $8 \times 10^{-9}$ mean contrast in the $360$ degrees dark hole with working angle between $3\,\lambda/D$ and $9\,\lambda/D$ using narrowband light centered at $516\,\text{nm}$. These materials were submitted on February 27, 2015 to the Technical Analysis Committee (TAC) and reviewed with the TAC March 13th.

This report is structured as follows. A brief HLC overview is provided in Sec. 2. Fabrication and characterization of the main starlight suppression component (the occulting mask) are presented in Sec. 3. HLC testbed hardware is described in Sec. 4, while wavefront control software is described in Sec. 5. The recent testbed results are reported in Sec. 6, while conclusions and future work are described in Sec. 7. We

caution the readers that yield estimations in Sec. 6.3 do not represent the expected WFIRST coronagraph instrument science yield and should not be used as such. Rather, we use this calculation as an engineering figure of merit for evaluating testbed progress, because it effectively compares the parameters of known Radial Velocity (RV) planets to both throughput and contrast as a function of the working angle of the coronagraph under test.

## 2 Hybrid Lyot Coronagraph Overview

As the light from the WFIRST-AFTA telescope is delivered to the coronagraph instrument, the first pupil is formed at the Fast Steering Mirror (FSM) that corrects the Line of Sight (LoS) pointing jitter and drift using information from the Low Order Wavefront Sensing and Control (LOWFS/C) subsystem. The light is then delivered to two Deformable Mirrors (DMs), which perform active wavefront control to compensate for phase and amplitude imperfections in the optical train. In the HLC case, they also have pronounced static surface settings that are a part of HLC's numerically optimized design and serve to control the diffraction from the WFIRST-AFTA pupil obscuration consisting of the secondary mirror and its supporting struts.

At the heart of the HLC is the focal plane occulting mask with numerically optimized layers of metal and dielectric.[1,2] The metal disc in the mask reflects the majority of the incoming on-axis starlight and diffracts the transmitted starlight so that it is blocked by the Lyot stop in a downstream pupil plane, while much of the slightly off-axis planet light is transmitted through the Lyot stop. A flip mirror can then send the planet light either to the imaging sensor for planet detection or to the Integral Field Spectrograph (IFS) for planet spectral characterization. The starlight rejected by the occulter is delivered the LOWFS/C subsystem[3] which uses it to measure the LoS pointing jitter and drift as well as other low-order wavefront error terms. Thus, the occulter is designed to perform two different functions: starlight suppression in transmission, and starlight phase modulation in reflection in order to enable the operation of the LOWFS/C.

## 3 Occulting Mask Fabrication

We have used two different processes to fabricate the HLC occulting masks. We describe each process in two subsections below.

### *3.1 E-beam lithography Fabrication Process*

The primary method is using an Electron-Beam Lithography (EBL) process utilizing the *JEOL 9300FS EBL* system at Microdevices Laboratory (MDL) in Jet Propulsion Laboratory (JPL). The nickel spot and profiled dielectric are fabricated in two separate but precisely aligned steps. The nickel spot is fabricated using a liftoff process as illustrated in Fig. 1. A bi-layer of two e-beam resists with different sensitivities is spin-coated on a fused-silica substrate. The bilayer serves to produce an undercut profile after e-beam exposure and development of the circular dot pattern. Nickel is then evaporatively coated over the entire wafer. The undercut resist profile produces a clean-edged nickel spot unconnected from the rest of the nickel, so that solvent can be used to dissolve away the resist and lift-off the unwanted nickel. Not shown in Fig. 1(a) are nickel crosses at the edge of the wafer that are in the same pattern as the nickel spots and serve as alignment marks for the dielectric e-beam exposure.

The dielectric used for the HLC masks is a polymer e-beam resist, MicroChem PMGI (polymethyl-glutarimide). The dielectric profiles are fabricated by direct-write analog e-beam lithography using the techniques detailed in [4, 5] and illustrated in Fig. 1(b). Briefly, the desired three-dimentional profiles are represented as floating-point depth patterns composed of $0.2\,\mu$m square pixels. JPL custom software is used convert the pixel depths into e-beam doses, including correction for the experimentally calibrated nonlinear depth vs. dose response of the PMGI resist and also the e-beam proximity effect (backscattered dose). Because the proximity effect deconvolution produces negative e-beam doses,[4] the entire pattern is recessed

until the minimum dose is within the capabilities of the EBL system. The corrected analog-dose pixel patterns were then converted using JPL software into native binary pattern files for the JEOL EBL system. When exposing the dielectric dose pattern, we utilize the EBL system's layer-to-layer alignment capability where it uses the beam to scan and precisely locate the position of the alignment marks fabricated in the nickel layer. After exposure, the resist was developed in an iterative manner using MicroChem 101A developer with depth measurement between steps to achieve accurate depth profiles. Fig. 2 shows a microscope photograph and an atomic force microscope surface profile of an e-beam fabricated HLC occulting mask.

### *3.2 Vacuum Deposition Process*

HLC occulting masks have also been fabricated using the vacuum deposition process. We have upgraded the vacuum deposition apparatus, which has been used to fabricate one-dimentional masks,[6] to be able to

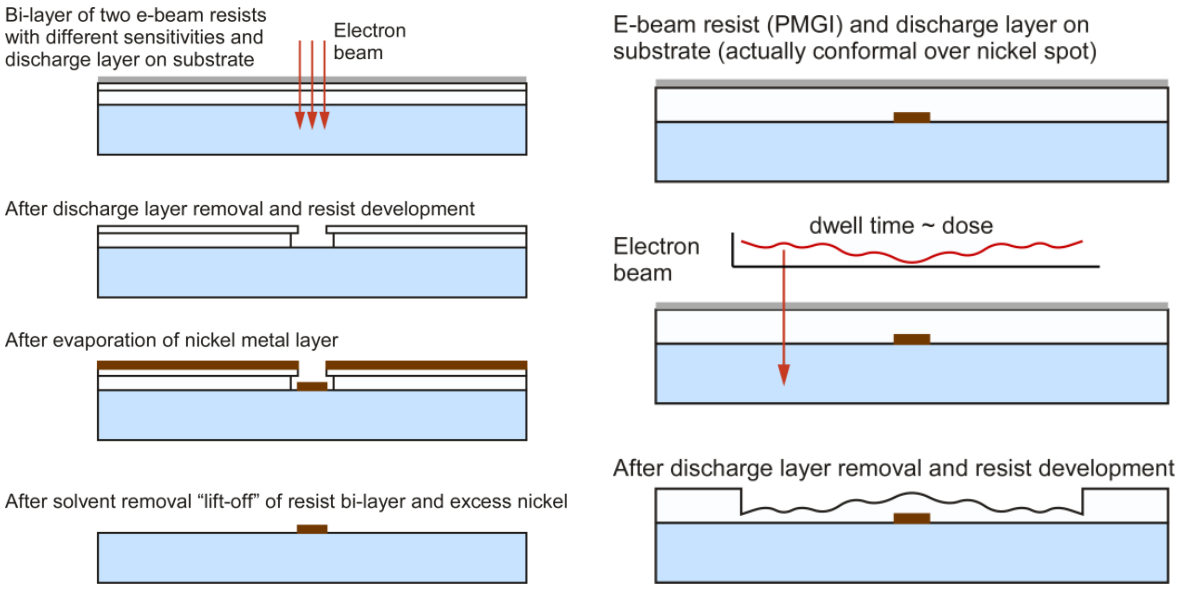


(a) (b)

**Fig 1** (a) E-beam liftoff process for fabricating the nickel spot, (b) E-beam process for fabricating the profiled dielectric on top of the nickel spot.

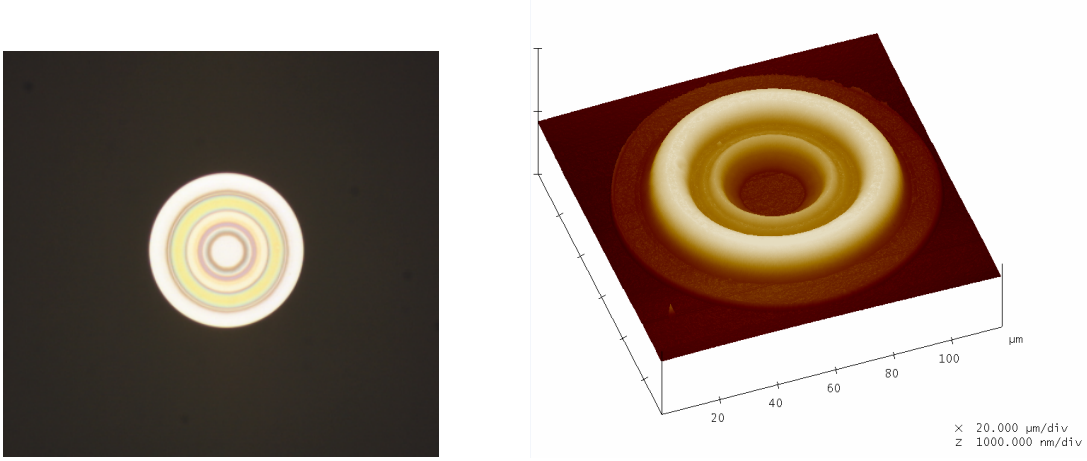


(a) microscope photograph (b) atomic force microscope profile

**Fig 2** HLC occulting mask using E-beam lithography process: (a) microscope photograph, (b) atomic force microscope profile.

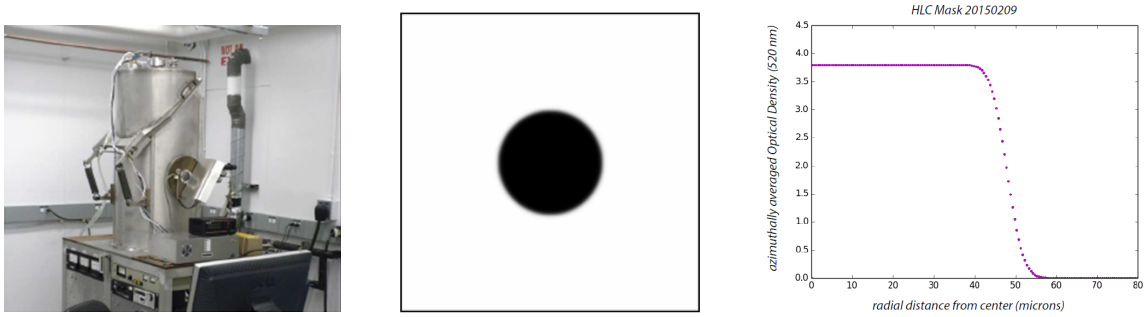


(a) (b) (c)

**Fig 3** HLC occulting masking using the vacuum deposition process: (a) photograph of the apparatus used, (b) microscope photograph of the Ni metal layer. Note that its edge can be apodized by by utilizing the stencil mask. (c) The measured profile of the Ni layer.

build two-dimentional structure. The apparatus is illustrated in Fig. 3(a). The vacuum deposition process relies on the direct e-beam evaporation of thickness-profiled metal and dielectric thin films onto a fused silica glass substrate. The deposition patterns are defined by a stencil mask placed between the deposition source and the glass substrate. The stencil mask is fabricated on a silicon-oxide-silicon wafer. The initial metal layer is composed of nickel with shape defined by a $48\,\mu$m diameter aperture in the stencil mask. The stencil and substrate are separated by approximately $0.001$ inches, creating a repeatable apodization of the circular edge. A microscope photograph of the Ni layer and its measured profile are illustrated in Fig. 3(b) and Fig. 3(c), respectively. Film thickness is monitored with a calibrated quartz crystal microbalance. A single thickness profiled layer of dielectric material is then deposited on top of the metal, this time using a $10\,\mu$m diameter aperture which is rastered in circular patterns to form the specified radial profile. Again, the separation between stencil and substrate create a repeatable apodization, which is accounted for in the mask design. The dielectric material can be either MgF2 or cryolite, materials that have nearly the same indices of refraction, hence are optically equivalent for our application. All materials are stable and robust for flight in a radiation environment.

## 4 Testbed Configuration

The HLC testbed was assembled on a $59'' \times 90''$ optical table inside a vacuum chamber in JPL's HCIT facility, where various other high-contrast imaging experiments have been demonstrated previously.[6–9] Fig. 4 shows the optical layout of the testbed. All flat mirrors are aligned mechanically using a Coordinate Measuring Machine (CMM) while all Off Axis Parabolas (OAPs) are aligned using an interferometer. Two $6'$ flat mirrors are used initially as surrogates of two DMs. After the alignment is finished, those two surrogates are replaced by the actual DMs.

The optical train begins with a $5\,$mW laser diode, which is located outside of the vacuum chamber. The center wavelength and bandwidth of the laser diode are measured as $516\,$nm and $1\,$nm, respectively. The light from the laser diode is carried in a single-mode fiber through a vacuum feedthrough, and illuminates a $3\,\mu$m diameter pinhole, which forms the testbed source (simulated star) and is located in the left of Fig. 4. The light then reaches the first DM (DM1) after being collimated by OAP1.

In front of DM1, an obscuration mask is placed mimicking the WFIRST-AFTA telescope pupil obscuration. The testbed photograph and its design are shown in Fig. 5(a) and Fig. 5(b), respectively. The physical gap between the unpowered DM surface and the mask surface facing DM1 is as small as $100\,\mu$m, thus, DM1 surface is essentially in the pupil plane and this obscuration mask forms the pupil stop of the testbed. The diameter $D$ of the clear area in the obscuration mask is $47\,$mm as shown in Fig. 5(a). The magnification between the pupil mask and the Lyot stop mask is designed to be $0.503$.

Then, the source is reimaged at the occulter after reflecting from the second DM (DM2), OAP2, and a fold flat mirror (FM1). DM1 and DM2 are separated by 1 meter and they are tilted by 9 degrees from the chief-ray.

Both DMs are identically designed $48 \times 48$ actuator AOX$^{TM}$ electrostrictive (Lead Magnesium Niobate or PMN) units, with 1 mm actuator pitch and a gold-coated fused silica facesheet.[6] These DMs have not been used in high contrast imaging testbeds before, although their $32 \times 32$ actuator and $64 \times 64$ actuator counterparts have been a part of every high contrast demonstration in HCIT in the past decade.[10] The DM1 has passed a flight-like vibration test performed at JPL in 2012. Their driving electronics (referred as "Generation 5 electronics") are newly designed and built to have non-multiplexed individually driving the

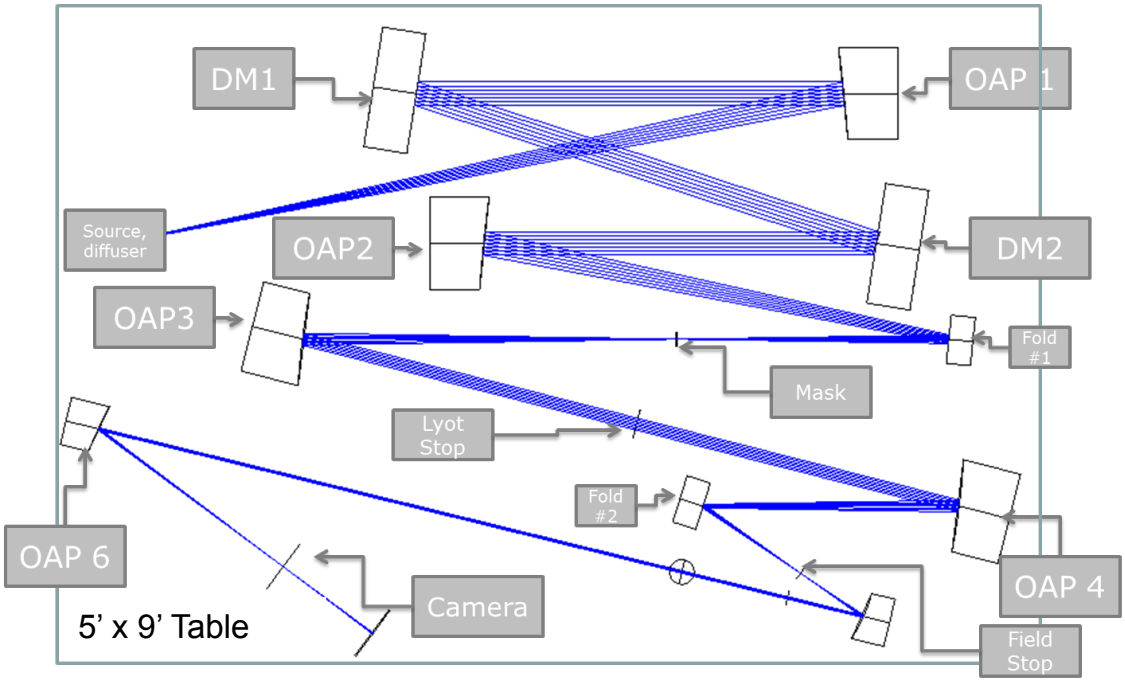


**Fig 4** The layout of the HLC testbed.

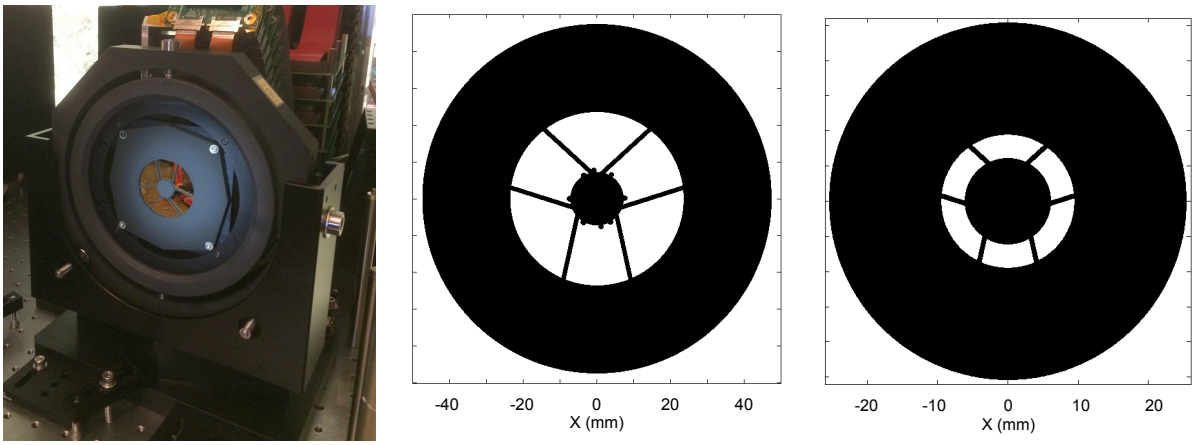


(a) (b) (c)

**Fig 5** WFIRST-AFTA obscuration mask and Lyot stop mask. (a) Testbed photograph of the WFIRST-AFTA pupil obscuration mask, which is mounted in front of DM1, (b) WFIRST-AFTA obscuration pupil mask design, and (c) Lyot stop mask design.

DM actuators at voltages between 0 and 100 Volts.

Occulters are mounted with fine-resolution x/y/z actuators along with coarse-resolution $4$ inch long translation stages, enabling us to test multiple occulters without breaking vacuum and opening the chamber. The occulter is also tilted by $5$ degrees, providing a separation angle between transmitted and reflected light. As described in Sec. 2, the HLC occulters are designed so that the reflected light is reused for the LOWFS/C, which is described in detail in [3]. Currently, a beam dump is placed instead of the LOWFS/C in the testbed. The backside of the occulter substrate is Anti-Reflection (AR) coated in the $500$-$600$ nm spectral range and the occulter is the only refractive optical element throughout the optical train.

The transmitted light through the occulter is recollimated and passes through a Lyot stop, whose design is shown in Fig. 5(c). The Lyot stop is a transmissive mask with a black painted metal frame. It is located in the conjugate plane of the pupil stop and is also tilted by $9$ degrees with respect to the chief-ray to match the DM1 tilt.

The collimated light after passing through the Lyot stop is refocused at the field stop. The field stop has simple circular shapes stopping the light outside the dark hole. Finally, the starlight reaches the camera after another relay of OAP5 and OAP6 at downstream of the field stop. The camera is mounted on a $10$ inch translation stage, permitting it to reach any planes covering both the pupil and focal planes indicated by black lines crossing the ray trace in Fig. 4. The translation camera stage also enables us to perform a phase retrieval technique as described in Sec. 5.1.

The HCIT-2 vacuum chamber typically reaches pressures around $1 \times 10^{-6}$ Torr. The chamber is floated (mechanically isolated from the ground) in typical operation. Inside the chamber, multiple accelerometers are attached next to major optical components, which monitors absolute and relative mechanical vibrations. The testbed is operated at the room temperature typically within $\pm$ $0.1$ degrees over $24$ hours. Multiple thermal sensors inside the chamber monitor these temperature changes.

## 5 Testbed Operation and Algorithm

The testbed operation largely consists of two different modes. The first mode is system characterization or calibration mode. In this mode, we perform the preliminary calibration such as establishing photometry, DM registration in the pupil plane, DM actuator gain measurement, and so forth. We perform this step as needed to update our knowledge of the testbed. The second mode is the Wavefront Control (WFC) mode to create a dark hole: a region where starlight is suppressed while off-axis planet light is visible. We describe the methods and algorithms we use in this mode in remainder of this section. Note that we employ the methods and algorithms developed and demonstrated before in the HCIT and described in detail by Kern, et.al.[7,8] although modifications were required to adjust to the system difference.

### *5.1 Phase Retrieval Algorithm*

Unlike other coronagraphs such as the Shape Pupil Coronagraph (SPC),[7] the DM shapes are one of the major design building blocks for the HLC.[1,6] That is, the DM facesheets have to be shaped properly to create a dark hole in conjunction with the hybrid occulter and the Lyot stop. We refer such a solution as "*DM solution*". In typical HLC testbed operation, the *DM solution* is initially generated by a representative computer model. When this *model-generated DM solution* is applied to the testbed DMs, the phase retrieval algorithm is utilized.

As discussed in Sec. 4, the translation camera stage enables us to take a series of images between pupil and focal planes. We use the modified Gerchberg-Saxton iterative solutions and nonlinear optimization of parametrized pupil-plane phase modes for the phase retrieval algorithm. We then estimate the pupil-plane phase with this phase retrieval algorithm. The phase retrieval algorithm has been utilized in other high contrast testbed demonstration.[7,8] Once the pupil-plane phase estimation is made, we iteratively change the applied DM actuator voltages to shape the wavefront phase, and obtain a new phase estimation, until the

wavefront is acceptably matched to the *model-generated DM solution*. Similarly, a "flat DM solution" can be obtained likewise, which provide acceptably flat wavefront at the occulter with the DMs compensating for wavefront imperfections introduced by other optical elements.

The phase retrieval algorithm is also utilized for various diagnostic and calibration process in the testbed such as obtaining DM actuator registration to the pupil and their individual voltages-to-facesheet displacement gains.

### *5.2 Wavefront Control (WFC)*

Just after the *model-generated DM solution* is applied to the testbed DMs, we observe that the contrast is typically worse than $1 \times 10^{-5}$. This is because of the following two reasons. First, there are some mismatches between the actual testbed and the computer model. It is difficult (or impossible) to capture all the details of the unavoidable testbed defects in the computer model to the level of obtaining high contrast directly after its application. Possible discrepancies include the occulter fabrication imperfections, optics misalignment, optics surface errors, and so forth. Second, it is also difficult to apply the *model-generated DM solution* into the testbed perfectly because of limitations of the phase retrieval algorithm or DM control.

Therefore, WFC is required to obtain high contrast in the testbed. We employ Electric Field Conjugation (EFC) for WFC process.[11] In EFC, we first establish the relationship between each differential DM actuator motion and the corresponding differential electric field in the dark hole at the given testbed state using a model. Then, we linearize this relationship and build a control matrix relating two quantities. The control matrix is used for determining the next DM setting to minimize the intensity inside the dark hole. Iteration is typically needed since the relation of these two quantities is nonlinear and the knowledge of the control matrix is imperfect.

In determining the next DM setting, a regularization parameter is included to weigh the relative importance of the DM actuator usage and the control gain. The regularization parameter is occasionally tuned by taking a series of extra images per iteration.

Once we have a reasonable dark hole in the testbed, we record that DM voltage setting and refer to it as the *testbed-generated DM solution* as opposed to the *model-generated DM solution*. Note that the *testbed-generated DM solution* is used for the initial DM setting for the consistency test as illustrated in Fig. 8.

### *5.3 Electric Field Estimation*

In addition to the control matrix, WFC requires estimation of the residual electric field in the dark hole region to determine the next DM actuator solution. We employ the pairwise estimation scheme[9] for the electric field estimation process. In this method, "probes" are placed on one of the DMs to modulate the electric field across the region of interest. The probes are applied typically in $\pm$ pairs, providing the largest phase diversity and probe simplicity as well as minimizing DM gain uncertainty impact. Given images corresponding to several probe pairs, along with an image with no probes applied at all, we can retrieve the complex electric field at the region of interest. Unlike the phase retrieval algorithm, no mechanical motion is required except DM actuators. Therefore, this estimation process is relatively quick and stable. However, prior testbed calibration is required to increase its accuracy such as the knowledge of the DM actuators registration to the pupil, their gains and photometry.

We employ three pairs of probes to cover the entire $360$ degrees region of the dark hole. In our case, probes are made from a combination of sinc and sine functions in the DM space (pupil space). These three pairs on the DM surface can be formulated as in Eq. (1).

$$\begin{cases} \delta h_e^{\pm}(x,y) & = \pm A \cdot sinc(2\pi f_w(x-x_o)) \cdot sinc(2\pi f_h(y-y_o)) \cdot cos(2\pi f_x(x-x_o)) \\ \delta h_o^{\pm}(x,y) & = \pm A \cdot sinc(2\pi f_w(x-x_o)) \cdot sinc(2\pi f_h(y-y_o)) \cdot sin(2\pi f_x(x-x_o)) \\ \delta h_c^{\pm}(x,y) & = \pm A \cdot sinc(2\pi f_h(x-x_o)) \cdot sinc(2\pi f_w(y-y_o)) \cdot sin(2\pi f_y(y-y_o)) \end{cases} \quad (1)$$

, where $x$ and $y$ are the coordinates representing one of the DM surfaces, $A$ is the probe strength, $f_w$ and $f_h$ are the probe width and height in the image plane, $f_x$ and $f_y$ are the probe center locations in the image plane, and $x_o$ and $y_o$ are the probe location in the DM plane. We refer to $\delta h_e^{\pm}$, $\delta h_o^{\pm}$ and $\delta h_c^{\pm}$ as *even*, *odd* and *cross* probe, respectively, as the subscripts of $e$, $o$, and $c$ denote. We typically use DM1 for the probing and we adjust the probe amplitude $A$ such that the resulting probe amplitude is comparable to that of the residual electric field amplitude in the dark hole.

Suppose $I_k^{\pm}$ is the corresponding intensity at the image plane when the $\delta h_k^{\pm}$ probe is applied. Fig. 6 shows the typical probe amplitude of the three probe pairs we measure in the testbed, which is formulated in Eq. (2).

$$\text{Probe Amplitude}_k = \sqrt{\frac{I_k^+ + I_k^-}{2} - I_o} \tag{2}$$

, where $I_o$ is the unprobed intensity.

As shown in Fig. 6, the probe amplitude of each pair is relatively uniform at the region of interest in the image plane. However, weak probing regions are also observed near the x or y axes. These weak probing regions are predicted due to the use of the sinc and sine/cosine combination of the probes. In order to have at least two strong probes amplitudes for all pixels, at least three pairs are required to provide full coverage over 360 degrees.

In addition to the complex electric field of the residual starlight, this algorithm also can find a portion of light that does not interact with the applied probes. We refer to this light as "unmodulated" or "incoherent" light. As the counterpart to the unmodulated light, we refer to the complex electric field of the residual starlight that responds to the probes as the "modulated" or "coherent" light.

Since the unmodulated light does not interact with the probes, its phase cannot be resolved, only its amplitude (intensity) is identified. Therefore, the WFC cannot correct the unmodulated light. The details are further described by Give'On, et.al.[9] Possible sources of the unmodulated light include non-stellar light, which is from light source other than the star, stray light and temporally unresolved light due to temporal variation such as vibration. As we discuss later in Sec. 6.2, this unmodulated light currently limits our contrast performance.

## 6 Testbed Result

### *6.1 Performance Summary*

Fig. 7(a) shows one of the raw high contrast images achieved in the testbed. The averaged raw contrast is $6.92 \times 10^{-9}$. We consider the full 360 degrees region between 3 $\lambda$/D and 9 $\lambda$/D. The narrow band light

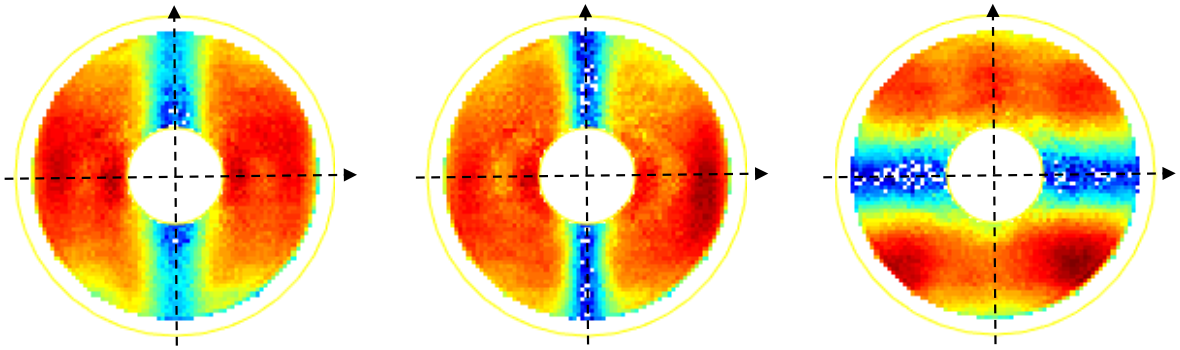

(a) even probe (b) odd probe (c) cross probe

**Fig 6** Probe amplitude of three pairs of probing in the dark hole region. These three pairs are required to estimate the electric field in the entire 360 degree area.

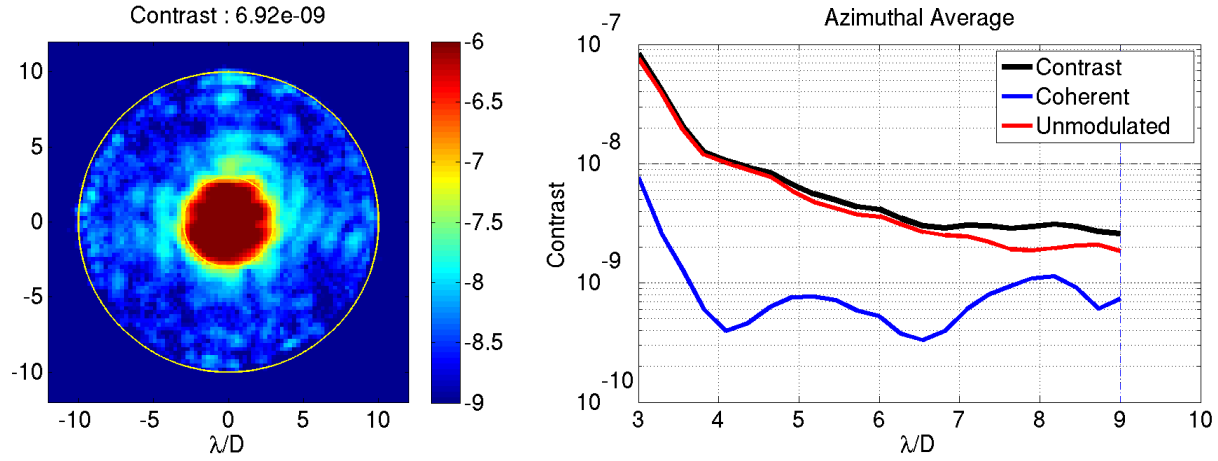


(a) (b)

**Fig 7** Averaged raw contrast of $6.92 \times 10^{-9}$ is obtained in this example considering the full 360 degrees region between 3 $\lambda$/D and 9 $\lambda$/D. The narrow band light centered at 516 nm is used and its spectral width is measured to be less than 1 nm. (a) 2D contrast image, (b) its azimuthal average. The black, blue, and red curves in Fig. 7(b) (and Fig. 8) denote the total, coherent, and unmodulated light components, respectively.

centered at 516 nm is used and its spectral width is measured to be less than 1 nm. In this particular case, we use an occulter fabricated by the e-beam lithography process described in Sec. 3.1. However, both occulters described in Sec. 3 provide similar level of contrast. The contrast accuracy is estimated to be less than 5 %, which is dominated by a photometry estimation uncertainty.

Achieved contrast performance is consistent and predictable as we can obtain repeated convergence below $8 \times 10^{-9}$ average contrast. Three independent WFC runs are demonstrated in Fig. 8. In each run, we start WFC from a *testbed-generated DM solution* described in Sec. 5. Getting the *testbed-generated DM solution* from the *model-generated DM solution* may require more iterations due the possible discrepancy between the model and the actual testbed as discussed in Sec. 5. However, once we obtain a *testbed-generated DM solution*, we achieve the dark hole contrast exceeding $1 \times 10^{-8}$ in fewer than 10 iteration cycles for every run, as shown in Fig. 8.

### *6.2 Performance Limitations*

The testbed performance is currently limited by the unmodulated light, which is defined in Sec. 5. Fig. 9 shows that the total residual contrast of $6.92 \times 10^{-9}$ is decomposed into the unmodulated (or incoherent)

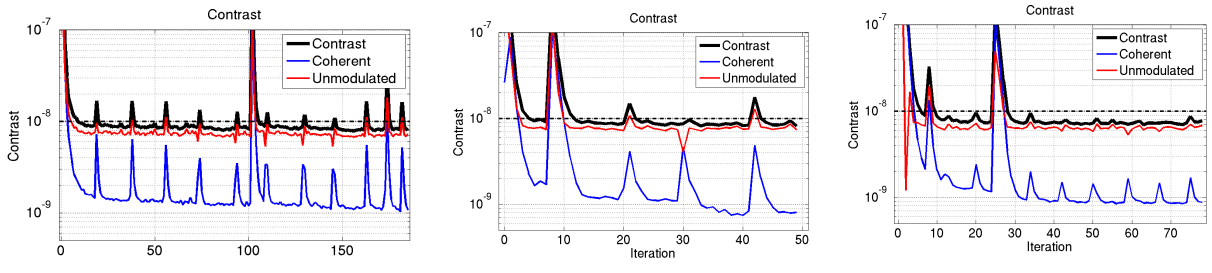


(a) (b) (c)

**Fig 8** Mean contrast across the dark hole as a function of WFC iteration number, for each of the three runs. The black, blue, and red curves denote the total, coherent, and unmodulated lights, respectively. See text for discussion of the sources of the contrast spikes.

light of $6.06 \times 10^{-9}$ and modulated (or coherent) light of $8.61 \times 10^{-10}$. Note that the modulated light is an order of magnitude smaller than the unmodulated light. The black, blue, and red curves in Fig. 7(b) and Fig. 8 denote the total, coherent, and unmodulated light, respectively, illustrating that the total contrast is dominated by the unmodulated light.

The sources of the unmodulated light have not yet been identified definitively. Nonetheless, we have indirect evidence that the testbed vibration (star vibration with respect to the occulter faster than our exposure time) is the dominant source responsible for this unmodulated light. Not having a direct measurement tool of the testbed vibration, we have indirectly measured the vibration of $0.2$ µm/axis RMS on the testbed occulter, which is equivalent to $0.5$ mas/axis RMS on sky for the WFIRST-AFTA telescope. The indirect methods include standard deviation measurement of the Point Spread Function (PSF) centroid motion as a function of the exposure time and the accelerometer measurement. Fig. 10 shows comparison between an unmodulated contrast image from the testbed and the computer simulation assuming the currently estimated vibration of $0.2$ µm/axis RMS. We observe a good morphological match between the two, showing that vibration can be the source of the unmodulated light. One of our near future tasks is to verify this by inserting a position sensing device at the occulter to measure the vibration directly.

The contrast spikes during the WFC iterations in Fig. 8 are due to two reasons. One is star adjustment to compensate for the testbed drift. We observe the testbed drift, which varies day by day from zero to typically $1$ µm per day. The amount and direction of the drift are well correlated to environmental change such as temperature and pressure. In order to overcome the drift, we employ an automated algorithm to monitor the drift and realign the star position periodically. Once the star drift is detected, the star adjustment is done only in the transverse direction (not along the beam propagation direction), typically on the order of $1$ µm, which corresponds to $\sim 1 \times 10^{-7}$ contrast, thus resulting several $\sim 1 \times 10^{-7}$ spikes shown in Fig. 8. The other smaller, more frequent contrast spikes come from a defect of the chamber floating system, namely a leak in one of the air legs, that causes it to ground periodically briefly shorting the chamber mechanically, before rising again. Nonetheless, these perturbation sources do not affect the resulting performance as WFC overcomes them and regains the high contrast after few iteration cycles as shown in Fig. 8.

### *6.3 Estimation of Yield*

We can estimate the science capabilities of WFIRST-AFTA flight mission based on the demonstrated laboratory contrast levels. The planetary targets are a list of 436 planets known from RV searches, referenced in [12]. From this RV planet target list, the parent star V magnitude and distance, and planet radius and semi-major axis are taken. A uniform $0.4$ albedo is assumed, and a phase angle for each planet's observation is chosen to be optimal for a $r^{-2}$ sensitivity (separation about $0.89$ of max elongation). From these values,

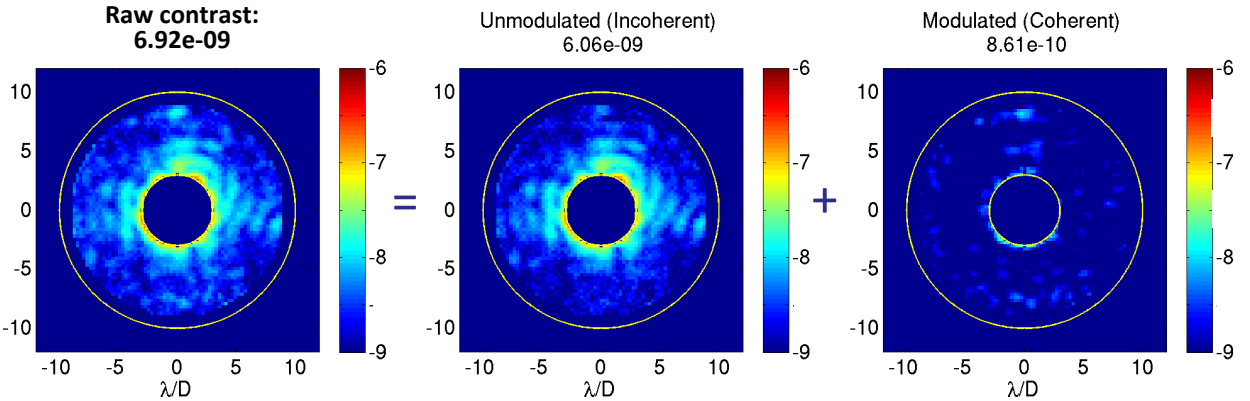


**Fig 9** Total contrast is decomposed into unmodulated and modulate light as descrivbed in Sec. 5. Current performance is dominated by unmodulated light.

an apparent separation and contrast are tabulated. Note that while eccentricities are determined from RV measurements, they are not used here, $\epsilon$ of 0 is used for simplicity.

Fig. 11 displays the RV targets plotted as contrast versus apparent separation. The demonstrated narrowband laboratory raw contrast level is overlaid as a solid line. The typical assumption for WFIRST-AFTA is that by post-processing (crudely, PSF subtraction), the raw contrast can be reduced to residual speckles that are fainter by a factor of either $10\times$ or $30\times$. When limited by these residual speckles alone, an Signal-to-noise ratio of 5 ($SNR = 5$) measurement can be reached for planets whose contrast is lower than the raw contrast by a factor of $10/5$ or $30/5$ after post-processing. The hatched region in Fig. 11 extends down to the lowest contrasts that can achieve a $SNR = 5$ measurement using $30\times$ post-processing.

To calculate the flux observable from a planet, the throughput of the system is estimated, assuming a 10 % fractional bandpass (appropriate to the mission expectations, but based on contrast numbers from the 1 nm bandpass used for this demonstration), 15 reflective surfaces with 97 % reflectivity each, and a detector Quantum Efficiency (QE) of 0.8. The total collecting area of the telescope, considering obscurations, is assumed to be $4.1\,m^2$. The planet PSF itself distributes light over large distances in the image plane, so only the "PSF core throughput" is considered to be relevant for planet measurements, as described in [13]. Combining these numbers, along with the parent star visual magnitudes and phase angle planet illumination, leads to the size of the planet symbols in Fig. 11. An observing time cutoff has been imposed where an $SNR = 5$ observation must take less than 24 hours, producing six blue circles in Fig. 11 for planets that meet the contrast requirement but do not meet the observing time cutoff.

Taken all together, the existing demonstrated narrowband contrast, extended to a 10 % broadband measurement and assuming a $30\times$ post-processing factor, would be capable of obtaining $SNR = 5$ measurements in less than 1 day each for 14 planets, with another 6 planets meeting the contrast requirement but not the observing time cutoff.

## 7 Conclusion and Future Work

WFIRST-AFTA mission is planned to include the first high-contrast stellar coronagraph in space that will directly image and spectrally characterize exoplanets around nearby stars. The HLC is one of the two modes of the baselined Occulting Mask Coronagraph (OMC) architecture, and is particularly advantageous for planet discovery due to the fact that it produces starlight suppression over full 360 degrees.

Substantial progress has been made in HLC component fabrication and experimental demonstration since National Aeronautics and Space Administration (NASA) selected the Wide-Field InfraRed Survey

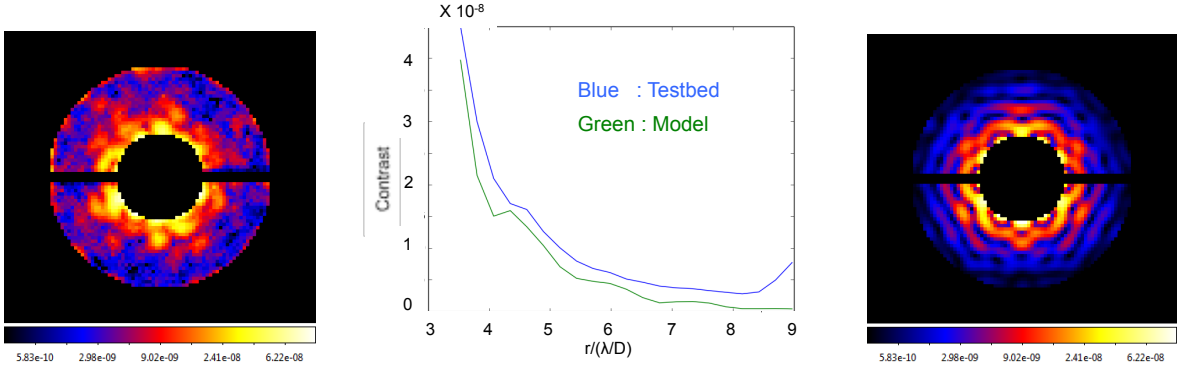


(a) Testbed Contrast (b) Azimual Average Comparison (c) Modeled Contrast

**Fig 10** Comparison between (a) an unmodulated contrast image from the testbed and (c) the computer simulation assuming that current estimation vibration of 0.2 µm/axis RMS is considered. Observed good match between two implies that vibration can be the source of the unmodulated light.

Telescope (WFIRST) coronagraph architecture in December 2013. A circular HLC occulting mask consisting of co-aligned metal and dielectric layers was successfully fabricated for the first time using e-beam lithography process. A high contrast HLC starlight suppression demonstration was performed in a vacuum testbed using two deformable mirrors for WFC in narrowband light. In presence of the obscured WFIRST-AFTA telescope pupil, we demonstrated consistently reaching starlight suppression better than $8 \times 10^{-9}$ averaged across the 3-9 $\lambda/D$ 360 degree dark hole. To the best of our knowledge, this is the highest contrast ever achieved over full 360 degrees in the presence of the telescope pupil obscuration.

The next experimental steps are to extend the starlight suppression demonstration to 10 % spectral band during 2015, and then, in 2016, to accomplish broadband starlight suppression in presence of simulated input wavefront disturbances expected to be experienced on-orbit by the WFIRST-AFTA observatory.

## 8 Acronyms



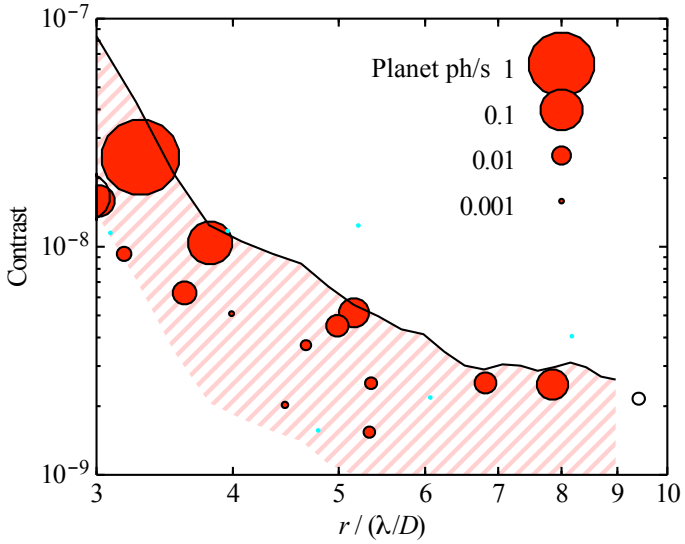


**Fig 11** Estimate of the science capabilities of an WFIRST-AFTA flight mission based on the demonstrated laboratory contrast levels.

**MDL** Microdevices Laboratory . . . . . 2
**NASA** National Aeronautics and Space Administration . . . . . 11
**OAP** Off Axis Parabola . . . . . 4
**OMC** Occulting Mask Coronagraph . . . . . 11
**PSF** Point Spread Function . . . . . 10
**QE** Quantum Efficiency . . . . . 11
**RV** Radial Velocity . . . . . 2
$SNR = 5$ Signal-to-noise ratio of 5 . . . . . 11
**SPC** Shape Pupil Coronagraph . . . . . 6
**TAC** Technical Analysis Committee . . . . . 1
**WFC** Wavefront Control . . . . . 1
**WFIRST** Wide-Field InfraRed Survey Telescope . . . . . 11

*Acknowledgments*

Presented WFIRST-AFTA coronagraph technology development work was carried out at the Jet Propulsion Laboratory using funding from NASA SMD and STMD. We acknowledge X. An, R. Diaz, D. Palmer, K. Patterson, D. Ryan, F. Shi, R. Zimmer and H. Tang for their contribution to testbed layout, assembly, and alignment, J. Krist for modeling advice, F. Greer, K. Balasubramanian, V. White, and R. Calvet for device fabrication, S. Macenka, and F. Zhao for programmatic advice.

*References*

1 J. Trauger, D. Moody, and B. Gordon, "Complex apodized Lyot coronagraph for exoplanet imaging with partially obscured telescope apertures," 2013.

2 J. Trauger, B. Gordon, J. Krist, and D. Moody., "Hybrid Lyot Coronagraph for WFIRST-AFTA: coronagraph design and performance metrics (To be published)," *Journal of Astronomical Telescopes, Instruments, and Systems Special Section, SPIE* , 2015.

3 F. Shi, K. Balasubramanian, R. Hein, R. Lam, D. Moore, J. Moore, K. Patterson, I. Poberezhskiy, J. Shields, E. Sidick, H. Tang, T. Truong, J. Wallace, X. Wang, and D. Wilson, "Low Order Wavefront Sensing and Control for WFIRST-AFTA Coronagraph (To be published)," *Journal of Astronomical Telescopes, Instruments, and Systems Special Section, SPIE* , 2015.

4 D. W. Wilson, R. E. Muller, P. M. Echternach, and J. P. Backlund, "Electron-beam lithography for micro- and nano-optical applications," *Proc. SPIE* **5720**, 2005.

5 D. W. Wilson, P. D. Maker, R. E. Muller, P. Z. Mouroulis, and J. Backlund, "Recent advances in blazed grating fabrication by electron-beam lithography," *Proc. SPIE* **5173**, 2003.

6 J. Trauger, D. Moody, B. Gordon, J. Krist, and D. Mawet, "A hybrid lyot coronagraph for the direct imaging and spectroscopy of exoplanet systems: recent results and prospects," 2011.

7 E. Cady, X. An, B. Balasubramanian, R. Diaz, J. Kasdin, B. Kern, A. Kuhnert, B. Nemati, K. Patterson, I. Poberezhskiy, A. Riggs, D. Ryan, H. Zhou, and R. Z. N. Zimmerman, "Milestone 2 final report: Shaped pupil narrowband contrast," *JPL Document* , 2014.

8 O. Guyon, B. Kern, A. Kuhnert, A. Niessner, and K. Balasubramanian, "Phase-induced amplitude apodization (piaa) technology development, milestone 1 monochromatic contrast demonstration," *JPL Document* **D-81778**, 2014.

9 A. Give'on, B. D. Kern, and S. Shaklan, "Pair-wise, deformable mirror, image plane-based diversity electric field estimation for high contrast coronagraph," *Proc. SPIE* **8151**, 2011.

10 P. R. Lawson, R. Belikov, W. Cash, T. Clampin, M. T. Glassman, O. Guyon, N. J. Kasdin, B. D. Kern, R. Lyon, D. Mawet, D. Moody, R. Samuele, E. Serabyn, D. Sirbu, and J. Trauger, "Survey of experimental results in high-contrast imaging for future exoplanet missions," *Proc. SPIE* **8864**, p. 88641F, 2013.

11 A. Give'on, B. Kern, S. Shaklan, D. C. Moody, and L. Pueyo, "Broadband wavefront correction algorithm for high-contrast imaging systems," 2007.

12 W. A. Traub, J. Breckinridge, T. P. Greene, O. Guyond, N. J. Kasdin, and B. Macintosh, "Science yield estimate with the WFIRST-AFTA coronagraph (To be published)," *Journal of Astronomical Telescopes, Instruments, and Systems Special Section, SPIE* , 2015.

13 J. Krist, "End-to-end numerical modeling of AFTA coronagraphs," *Proc. SPIE* **9143**, p. 91430V, 2014.